Volume 18 | Number 5 | 07 March 2018 | Pages 691–842

Lab on a Chip

Devices and applications at the micro- and nanoscale

rsc.li/loc

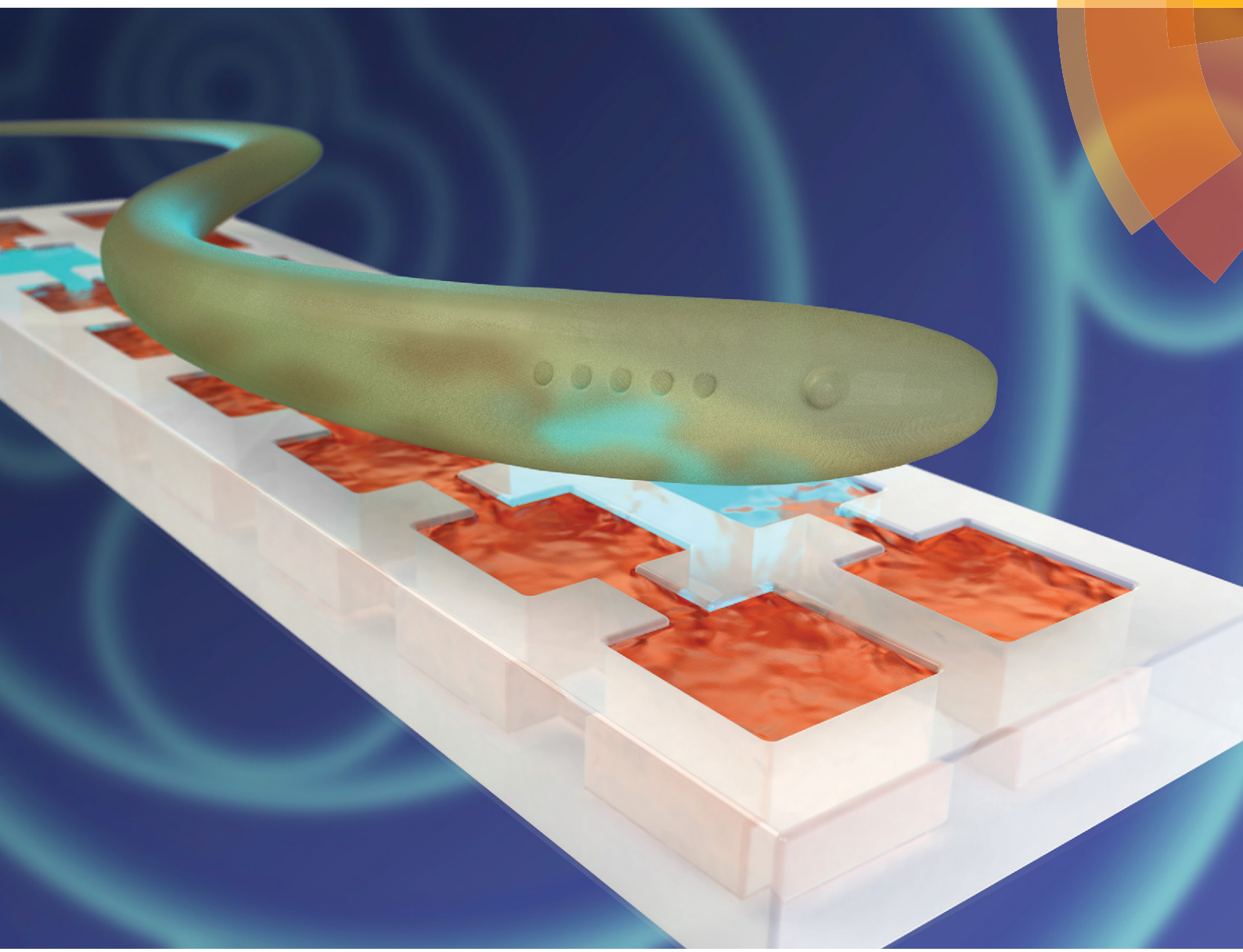

ISSN 1473-0197

ROYAL SOCIETY OF CHEMISTRY

PAPER

Seth Fraden *et al.*

Engineering reaction–diffusion networks with properties of neural tissue

Lab on a Chip

PAPER

Check for updates

Cite this: *Lab Chip*, 2018, **18**, 714

Engineering reaction–diffusion networks with properties of neural tissue†

Thomas Litschel, ‡ Michael M. Norton, Vardges Tserunyan and Seth Fraden *

Received 7th November 2017,
Accepted 15th December 2017

DOI: 10.1039/c7lc01187c

rsc.li/loc

We present an experimental system of networks of coupled non-linear chemical reactors, which we theoretically model within a reaction–diffusion framework. The networks consist of patterned arrays of diffusively coupled nanoliter-scale reactors containing the Belousov–Zhabotinsky (BZ) reaction. Microfluidic fabrication techniques are developed that provide the ability to vary the network topology and the reactor coupling strength and offer the freedom to choose whether an arbitrary reactor is inhibitory or excitatory coupled to its neighbor. This versatile experimental and theoretical framework can be used to create a wide variety of chemical networks. Here we design, construct and characterize chemical networks that achieve the complexity of central pattern generators (CPGs), which are found in the autonomic nervous system of a variety of organisms.

Introduction

Central pattern generators are a class of neural networks found in the autonomic nervous system that perform cyclic functions and govern motions such as swimming, walking, and the peristaltic motion of the digestive system. The networks produce rhythmic pulses distributed in space that coordinate muscle contractions (Fig. 1). Minimal models treat individual neurons as self-driven non-linear oscillators that when coupled together produce complex spatio-temporal patterns.[1,2] Turing recognized that chemical reactions were capable of producing self-driven oscillators and elucidated the conditions in which diffusively coupled chemical networks exhibit spontaneous spatio-temporal pattern formation.[3] Guided by this insight, we seek to leverage the self-organizing properties of reaction–diffusion systems to engineer a synthetic substrate that emulates the autonomous pattern formation exhibited by central-pattern generators. In this paper, we describe the design and fabrication of a network of coupled chemical oscillators that generates the spatio-temporal pattern produced by a swimming lamprey (Fig. 1).

As the name implies, reaction–diffusion networks have two components. The term *reaction* refers to the chemistry. As a first step of the design process we, like Turing, idealize the chemical kinetics as taking place inside a single reactor, disregarding spatial extent. The term *diffusion networks* refers to the physics with a focus on the spatial structure and interconnectivity of the network as characterized by (i) the topology of the network, the (ii) boundary and (iii) initial conditions, (iv) the volume of each reactor, (v) the coupling strength, and (vi) whether the coupling is of an inhibitory or excitatory nature. To enable the rational engineering of reaction–diffusion networks it is important to have control over each of these factors.

We utilize the Belousov–Zhabotinsky (BZ) reaction, a non-linear chemical oscillator. The BZ reaction is a metal ion-catalyzed oxidation of an organic substrate, in which chemical concentrations of intermediate reactants and products oscillate over time.[4,5] The simplest description of this oscillatory reaction is with two principle components; an autocatalytic activator that drives the catalyst to the oxidized state and an inhibitor that returns the catalyst to the reduced state.[6–8] The ability of the BZ chemistry to operate in either an oscillatory/limit-cycle or excitable regime makes it a prime analogue for neurons. The parallel between the two systems has been appreciated and leveraged to produce neuro-mimetic systems by linking together stirred reactors *via* reagent pumps.[9] Pattern formation in larger networks of photo-chemically linked catalyst-laden beads and gels have been observed as well.[10–12] While these examples demonstrate the strength of BZ as a model oscillator, the systems do not possess inherent dynamics that are independent of the electrical, mechanical and optical controllers responsible for inter-oscillator coupling and are therefore not suitable for the creation of autonomous materials with intrinsic pattern formation.

Department of Physics, Brandeis University, Waltham, MA 02453, USA. E-mail: fraden@brandeis.edu

† Electronic supplementary information (ESI) available. See DOI: 10.1039/c7lc01187c

‡ Current address: Max Planck Institute of Biochemistry, Martinsried, 82152, Germany.

This journal is © The Royal Society of Chemistry 2018

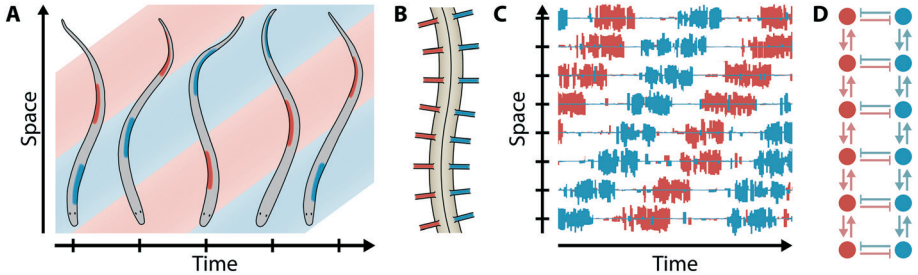

Fig. 1 Example of a biological central pattern generator.[1] (A) Lampreys swim by generating waves of transverse displacement down their spinal column. Red areas indicate regions of muscle contraction left of the spinal cord, blue indicates regions of muscle contraction right of the spinal cord. (B) Schematic diagram of an exposed lamprey spinal cord with ventral roots. Each vertebra has a pair of neurons, situated to the left and right of the column. (C) Schematic time trace of electrical activity for each of the corresponding pairs of ventral roots shown in (B). In red (blue) traces show the voltage of neurons on the left (right) side of the spinal cord. Neurons on opposite sides of a vertebra fire with a relative phase shift of 180°, while neurons on the same side fire with a small phase lag between neighboring vertebrae, producing the displacement wave shown in (A). (D) Schematic of lamprey central pattern generator realized as a reaction–diffusion network. Each circle represents an oscillating chemical reaction. Links with nails (arrows) indicate inhibitory (excitatory) coupling.

In recent years, the Belousov–Zhabotinsky (BZ) reaction encapsulated in emulsions of droplets with diameters in the 100 μm range has emerged as a powerful experimental system to study reaction–diffusion networks. The state of the art of BZ networks up to the year 2017 has been reviewed in an article in *Lab on a Chip*; "Chemical communication and dynamics of droplet emulsions in networks of Belousov–Zhabotinsky micro-oscillators produced by microfluidics".[13] In two-dimensions (2-D) it is possible to create networks of varied topology and, using a photo-sensitive catalyst, set initial and boundary conditions.[14] Thus, diffusion network properties (i–iii) have been achieved. However, while small networks of drops of different volume have been formed in multiple emulsions, network topology and volume cannot be independently varied using this method.[15] Additionally, control of coupling strength is limited and means are lacking for specifying whether a particular link between drops in BZ emulsions is excitatory or inhibitory. Thus, properties (iv–vi) remain to be developed. The aim of this work is to create BZ reaction–diffusion networks in which all the diffusion network properties, (i–vi), can be realized and to exploit these properties to engineer non-trivial reaction–diffusion networks.

Experimental methods

Surfactant stabilized emulsions consisting of aqueous BZ droplets in a continuous phase of oil allow only a subset of the BZ reactants to diffuse from drop to drop. Depending on the BZ conditions and how the BZ chemicals react with the oil and surfactant, coupling is either dominated by bromine, Br_2, an apolar molecule, which in the simplified classification, acts as an inhibitor,[14,16–22] or coupling is dominated by excitatory species.[19,23] Other ways to induce excitatory coupling are to immobilize the catalyst in specific sites and then allow all the BZ reagents minus the catalyst to diffuse over the sites.[24,25] Thus, while there are several systems which allow either all the links in a reaction–diffusion network to be excitatory or all the links to be inhibitory, there are no BZ networks for which each individual link can be specified as being either excitatory or inhibitory.[13]

To create a network in which each link can either be excitatory or inhibitory, we replace the liquid oil used previously in the BZ emulsion system[14,16–21] with the solid elastomer polydimethylsiloxane (PDMS). The oils used in emulsions and the elastomer PDMS have similar dielectric constants. Additionally, only 10% of the PDMS is cross-linked. Therefore, at a molecular scale, the majority of the elastomer resembles the fluid oil and consequently, the permeation and diffusion constants of BZ chemicals in PDMS and oil are similar.[18,26,27] Similarly to BZ emulsions, we found that adjacent BZ wells that were separated from each other by a wall of PDMS (Fig. 2A) were inhibitory coupled. Excitatory coupling was accomplished by building thin channels between wells (Fig. 2B). Wells connected by narrow channels allow the propagation of chemical waves, a phenomena characteristic of bulk, excitable BZ solutions.[26] Substantive advantages of PDMS confinement of BZ reactions over that of previous emulsion methods are that extensions of soft lithography methods greatly eases compartmentalization of BZ solution in PDMS wells of arbitrary size, shape and location in 2-D and allows selection of coupling type.

To pattern these nanoliter-scale wells into thin sheets of PDMS, we optimized existing microfluidic fabrication techniques[14,28] (Fig. S1A†). Crucial to the fabrication of the networks is to minimize the layer of PDMS at the bottom of each well (Fig. 2). The bromine produced by the BZ reaction partitions into this space,[26,27] and the reaction stops if the ratio of PDMS to BZ exceeds about 5 : 1,[14] because a critical concentration of bromine is necessary to sustain the reaction. Therefore, we fabricate PDMS sheets in which the thickness of the bottom of the well is less than 1 micron (Fig. S2†). After immersing the wells in BZ solution, we seal the filled BZ compartments air-tight with a glass lid (Fig. S3†) to prevent nucleation of CO_2 bubbles, which are a nuisance that often plague BZ experiments.[29] Manufacturing protocols for

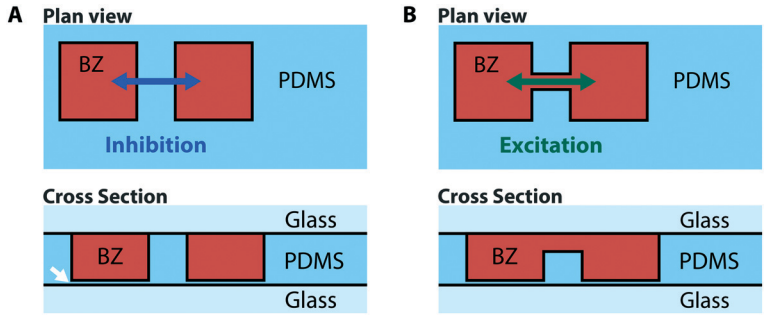

Fig. 2 Inhibitory and excitatory coupled BZ reactors. Plan and section views of two compartments that are designed to be inhibitory coupled (A) or excitatory coupled (B). BZ solution in red, PDMS in blue, glass in light blue. Diffusional coupling is indicated by double-arrows. It is important to minimize the thickness of PDMS below each well (white arrow) during fabrication (see Fig. S2†).

high-yield device fabrication are documented in Movies S6 and S7 and in the ESI.†

Our engineering design is guided by considering reaction–diffusion systems as being described by partial differential equations whose spatio-temporal behavior is a function of boundary and initial conditions. To control (ii) boundary and (iii) initial conditions, we include the photosensitive catalyst tris-(bipyridine)-ruthenium(II) ($[Ru(bpy)_3]^{2+}$) in the BZ solution. Essentially, when illuminated with blue light, a $[Ru(bpy)_3]^{2+}$-BZ solution is prevented from oscillating and is set in partially oxidized steady state.[30] We utilize a homemade programmable illumination microscope (PIM)[31] for a light source. This microscope has two illumination arms; one to control the chemical reaction and one to observe the oxidation state. The control arm consists of a computer projector capable of projecting blue light with wavelength centered at 450 nm at arbitrary locations over the entire field of view and allows the intensity of each pixel to be varied in time.[14,31] The observation arm utilizes Kohler illumination at 510 nm to maximize the contrast of the ferroin dye that indicates the oxidation state of the $[Ru(bpy)_3]^{2+}$ catalyst.[14,18]

To establish defined boundary conditions, we fabricate an additional structure (a moat) in the PDMS containing BZ that surrounds, but is not directly connected to the network of interest (Fig. 3A). The BZ chemical composition is initially the same in all structures, but using the PIM to illuminate the BZ in the moat with sufficient light moves the reaction off the limit cycle, fixing the reaction in a stationary state of constant chemical concentration, including a fixed bromine concentration. This establishes a well-controlled, time-invariant boundary condition consisting of constant chemical concentrations in a region surrounding the network under study.[14,18,21] The non-illuminated wells continue to oscillate, while the surrounding illuminated moat isolates the network from the environment. Without the light controlled boundary conditions, a small array of BZ wells, such as illustrated in Fig. 3 would exhibit transient behavior due to mass transfer of bromine from the well into the surrounding material beyond the moat, which constitutes a much larger volume than the nanoliter-wells containing the BZ solution.

We impose initial conditions by illuminating each well individually and then extinguishing the light on different wells. If the light is removed from all the wells at the same time, then the wells begin oscillating in-phase. If the light is removed at different times, then the oscillations in different wells have a phase shift proportional to the time of light removal. Once the light is removed, the BZ reaction commences and rapidly reaches the limit cycle in the reduced state. Oscillations begin approximately half an oscillation period after removal of light.

Results

Spatial control of wave speed in linear arrays of wells

We constructed linear arrays of wells connected by small channels in the manner shown in Fig. 2B. Fig. 4 shows such

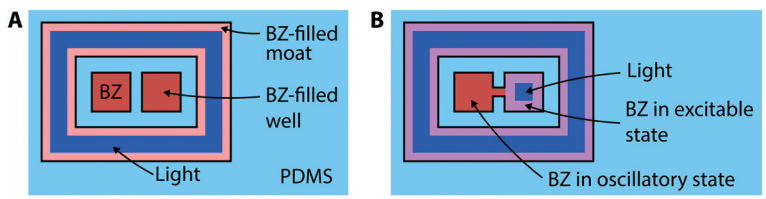

Fig. 3 Boundary conditions and pacemakers. (A) Two BZ filled wells (red) surrounded by a BZ filled moat. Blue light (blue frame) sets the BZ in the moat in an oxidized stationary state (light red). (B) Two BZ filled wells with a channel connection, surrounded by a BZ filled moat. The right well and the moat are exposed to light (blue square and blue frame, respectively). If the light intensity is low enough, the BZ reaction is set into a non-oscillatory, but excitable state (purple). Oscillations in the surrounding moat are still suppressed; but activator from the oscillating left well ("pacemaker well"), can diffuse through the channel and oxidize the BZ in the right well.

 This journal is © The Royal Society of Chemistry 2018

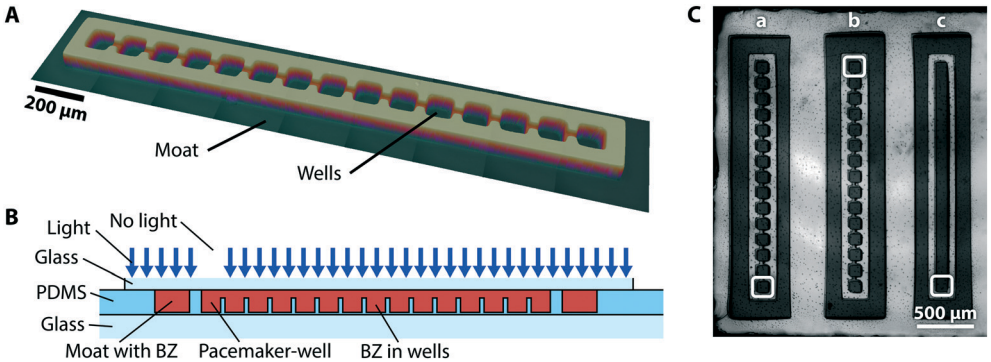

Fig. 4 1-D arrays of wells. (A) Image of a row of wells fabricated in PDMS interconnected by channels taken with an optical profilometer and rendered in false color. (B) Schematic of cross section along the chain of wells. Dimensions not to scale. (C) Photograph of PMDS wells filled with BZ solution and surrounded by moats to establish constant chemical boundary conditions. The left (a) and the middle array (b) are geometrically identical arrays consisting of fifteen wells connected by channels. On the right (c) is a continuous chamber. Pacemaker wells, uninhibited by light, are located on alternate ends of each array and are indicated by white boxes. Movie S1† shows an experiment with propagating waves in each array.

a design. Well dimensions were held constant 100 μm × 100 μm × 110 μm ($L \times W \times H$) while the widths and heights of the connecting channels were varied. We explore the engineering of excitatory connections by investigating the dependence of wave speed on geometry. We expected that the abrupt change in channel width would induce a curvature in the wave front as it emanates from the small channel into the large well, which causes the wave to slow down according to previous experiments that were explained theoretically by the Eikonal equation.[26,32–34] This well-established phenomena occurs when an isolated reaction–diffusion wave front emerges from a small channel into a large volume and thereby acquires a curvature (circular in 2-D and spherical in 3-D); curved reaction–diffusion fronts dilute the activator responsible for propagating the reaction front, subsequently reducing wave speed. As the wave front advances into the well and interacts with the wall, the curvature reduces and concomitantly the wave speed increases. Instead, as described below, we found the opposite behavior occurred; wave velocity increased upon exiting a small channel into a larger one.

To set the direction of wave propagation, we illuminate all but one of the wells on one end of the 1-D array. The un-illuminated well oscillates spontaneously and serves as a "pacemaker" (see Fig. 3B and 4B). The light intensity is strong enough to suppress spontaneous oscillations in the illuminated wells, but weak enough such that they are still excitable and oxidize when they receive activator from a neighboring well. Such a technique has been used to study wave-propagation in continuous media.[35] Using a pacemaker allows for repeatable experiments, but is also a necessary control feature for the biological central pattern generator neural network shown in the introduction. We program pacemakers in adjacent channels to be located at opposite ends of the channels (Fig. 4C), which causes the waves to propagate in opposite directions. Comparing the resulting wave speeds controls against possible undesirable experimental gradients, such as uneven illumination. With each experiment, we include a continuous channel, which can be considered as an array with channels of maximal width and height (Fig. 4C, right). The continuous channel provides both a control and a reference velocity c_0 by which to normalize wave speeds through corrugated channels.

A space–time plot, Fig. 5B, shows the discretized nature of the wave as it moves from well to well. The near vertical slope in the space–time plot conveys that the wave speed inside a wide, deep well (yellow) is much greater than both the average wave speed (green) and the speed in a narrow, shallow channel between wells (red). While the contrast in the experimental space–time plot doesn't allow us to show the signal within the channels, the offset between the signals in neighboring wells indicates a time delay from which we infer a slower wave front speed. Movie S1† shows a recording with 3 simultaneous, but independent experiments; the wave speeds of each propagating wave are shown in Fig. S4A.† The system-average wave speeds of each experiment are constant over time, establishing that the experiments have reached steady state. As an aside, comparison with Fig. S4B† reveals a similar dependency on geometry for experiments without a pacemaker well created by light. However, these experiments lacked spatial control over the wave origin and we observed waves would simultaneously randomly initiate in multiple wells.

The main experimental trend is that wave speed increases with increasing cross section of the connecting channels (Fig. 6A). The Eikonal equation predicts that the speed of isolated plane waves should be the same in long uniform channels independent of width, as is borne out in our finite element simulations (Fig. S5†). However, Fig. 7 shows that the wave speed is fast in the wide uniform-width well and slow in the narrow uniform-width connection. This is because the periodicity of the spacing of the wells is close to the width of the wave front (Movie S2†). Thus the assumption of isolated plane waves breaks down and the Eikonal equation prediction no longer holds.[33,34] In contrast, Ginn *et al.*[26] observed that the wave speed slowed down when transitioning from a narrow to wide channel, consistent with the

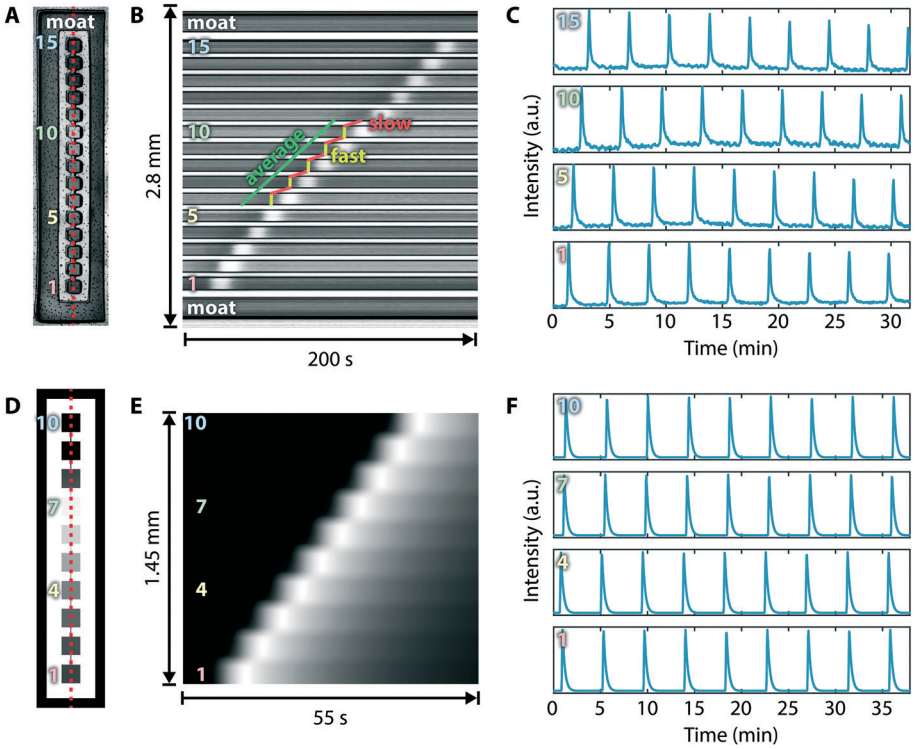

Fig. 5 Waves in 1-D arrays of wells. (A) Photograph of a linear array of 15 connected wells filled with BZ solution. Well 1 is the un-illuminated pacemaker well (see Fig. 4B). Once the wave is initiated in the pacemaker, it travels towards well 15. Shown is the left array in Movie S1.† (B) A space–time plot is generated by plotting the intensity recorded along the red dotted line in (A) as a function of time. A single propagating wave is plotted. The intensity is proportional to the concentration of oxidized catalyst and the duration of a single oxidized pulse is about 15 seconds. The rows in (B) are aligned with the corresponding wells in (A) and share the same numbering. For example, the intensity of well 5 in (A) is plotted as a function of time in row 5 in (B). The leftside of the bright pulse in row 5 corresponds to the leading edge of the wavefront entering well 5, while the rightside corresponds to the trailing edge of the wave front leaving well 5 at a later time. The slopes of the superimposed colored lines are equal to the wave speeds. The wave front propagates rapidly through the wide wells, as represented by the steep yellow line and slowly through the narrow channels as shown in red. In the latter, front propagation is not visible due to low contrast in the channels and the propagation speed is inferred by connecting fronts of the two adjoining wells. The average speed is shown in green. (C) Intensity traces of 4 selected wells. Numbers in the top left corners refer to position of the wells in the array. Nine oscillations are shown in (C), while only one is shown in (B). The pulses are asymmetric, with steep leading edge and a long tail to the trailing edge. (D to F) 2-D finite element simulation of the experiment shown in (A to C). Shown is the concentration of oxidized catalyst (white: high concentration; black: low concentration).

Eikonal equation. This is because the length of the channels was much greater than the width of the wave front, closer to the idealized case described by the Eikonal equation.

We compare our results to 2-D finite element method (FEM) simulations to better understand the relationship between geometry and wave speed. The green curve in Fig. 6A shows the calculated normalized, predicted wave speed as a function of channel width. While the 2-D Field–Korös–Noyes (FKN)[5] model overpredicts the measured 3-D wave speed by a factor of ~2.5, comparing normalized results demonstrates that our model captures the overall geometric dependence. Movie S2† shows FEM simulations of wave propagation through a linear array for the case of a 10 μm connecting channel (color map corresponds to the oxidized catalyst concentration).

For very small channel sizes, we found that only every other wave propagates to the end of the array. Furthermore, the distance the disrupted waves propagate before termination shows a pattern that repeats every 4 cycles (Fig. 6B and C, and Movie S3†). These periodic behaviors are sensitive to the amount of light we apply to suppress free oscillations. Similar periodic phenomena have been reported for other BZ systems.[15,36,37] Additional quantitative information about the period of oscillations as a function of time in experiment and the spatial dependency of propagation speed in experiment and theory can be found in Fig. S4(C to F).†

Given the importance of boundary conditions for reaction–diffusion systems, we calculated FEM-predicted wave speed for bromine-permeable walls in order to model the experimentally utilized PDMS channels. For comparison, we also employed no-flux walls, which model glass or silicon devices, to explore the role of boundary conditions on wave speed. We were surprised to find only a small difference in wave speed of at most a few percent between the bromine permeable and bromine impermeable channels (Fig. S4G†).

Previous researchers noticed how bromine-permeable PDMS affects BZ chemical dynamics. Buskohl and Vaia[27] used PDMS to control initial conditions. By placing PDMS walls in contact with a BZ gel, they generated a bromine sink that disinhibited a specific region. This creates a pacemaker

 This journal is © The Royal Society of Chemistry 2018

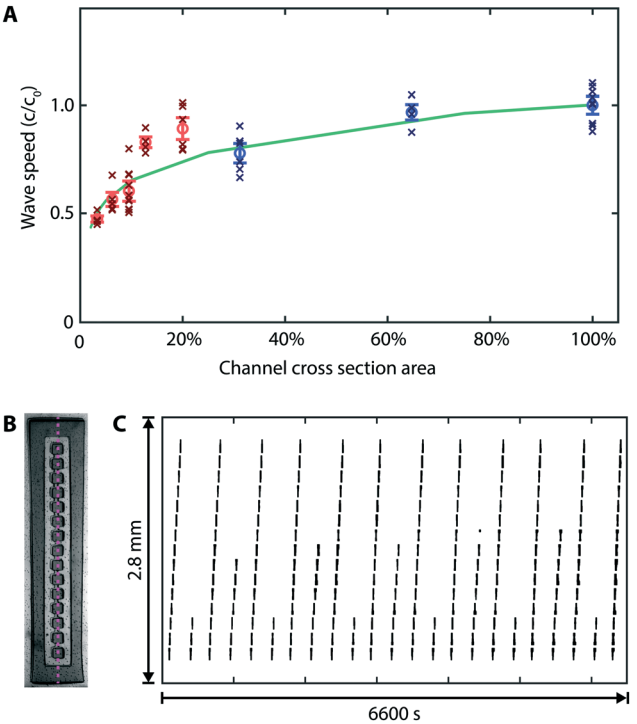

Fig. 6 Channel size dependency of wave speed. (A) Dimensionless wave speed c/c_0 *vs.* channel cross section for theory and experiment (48 individual experiments). Well dimensions were constant; 100 μm × 100 μm × 110 μm ($L \times W \times H$). Red: channel width of 20 μm and varying channel height. Blue: channel width of 100 μm and varying channel height. Crosses: measurements, circles: average velocities, error bars: standard deviation. Green line: 2-D finite element simulations of wave speed *vs.* channel cross section. Measurements in 3-D and theoretical predictions in 2-D are normalized by their respective values for a continuous channel: $c_{0,exp}$ = 27.7 μm s^{-1} and $c_{0,fem}$ = 74.1 μm s^{-1}. Photograph (B) and space–time plot (C) of chemical waves in a linear array with small channels of 6% cross-section. The pink line in (B) indicates the spatial component of the space–time plot. Half of the waves terminate before reaching the end of the array. The termination location repeats every 4 cycles. The experiment is shown in Movie S3.†

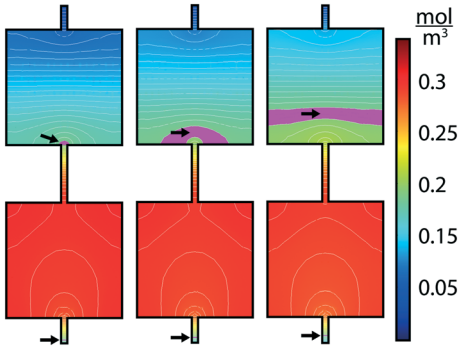

Fig. 7 FEM simulation of wave propagating through connected wells. Activator concentration (red: high, blue: low) calculated by FEM simulation at three, equally spaced times. Black arrows point to the magenta contour, arbitrarily chosen to be half the maximum activator concentration, which highlights the advancing (wide channel) and receding (narrow channel) wave fronts. The wave front in the wide channel advances much further than the wave front in the narrow channel over the same time intervals. See Movie S2.†

by locally absorbing bromine. However, the bromine concentration in the PDMS will increase with time until the bromine reaches the outside of the PDMS and encounters a new boundary condition. Thus, PDMS on its own does not constitute a time-independent boundary condition. This is in contrast to the photo inhibited moat (Fig. 3A); as long as the light shone on the moat is constant, the chemical composition of the moat will also be constant.

Ginn *et al.*[26] measured the wave speed in a narrowing PDMS channel and observed that the speed increased as the channel width decreased. This phenomenon was explained as arising from the permeation of the inhibitor bromine into the PDMS, thereby disinhibiting the BZ reaction. Narrow channels have more disinhibition than wide channels due to the larger surface to volume ratio. In contrast, in our wave speed experiments and simulations, the wave speed was slower in the narrow section (Fig. 5 and 6). Additionally, in our simulations the wave speed was the same for bromine permeable and impermeable channels (Fig. S4G†). The differences between previous observations of wave speed in PDMS channels[26] and our work is that we employ spatially modulated channels whose wave length is approximately equal to the width of the wave front. In such cases, it has been shown that the wave speed is greatly reduced, even to the extent of blocking wave propagation.[33,34] This suggests that the wave speed in the case we studied is controlled more by channel geometry than by channel composition. This has important engineering consequences for designing autonomous networks in which wave speeds vary in different locations because it is much easier to lithographically fabricate networks with spatially variable geometry than to engineer networks with spatially variable chemical composition.

Central pattern generator

Thus far in this paper we've established the ability to control initial and boundary conditions, wave speed, and create pacemaker nodes. We conclude by adding an additional feature: well-coupling through the inhibitor (Fig. 2A). In previous works, we explored inhibitor-coupling at length using fluorinated oils as the interstitial medium; here, we implement inhibitor-coupling for the first time using PDMS elastomer and demonstrate that both materials function identically in that the dynamic attractor for two oscillators is 180° out-of-phase, also known as anti-phase synchrony. We use these engineering principles in concert to design and fabricate a central pattern generator circuit inspired by the lamprey and illustrated in Fig. 1.

This neural network is responsible for autonomous muscle control in a variety of organisms.[38,39] The CPG's function is to initiate waves of muscle contractions that alternatively travel down the left and right sides of the spinal column, giving rise to the sinuous motion of the lamprey as illustrated in Fig. 1A.[2,38] The minimal model that produces this

behavior is that of two parallel chains of oscillators, shown in Fig. 1D.[1] Fig. 8A shows the BZ implementation in which structure implies function. It is comprised of two identical linear arrays of BZ oscillators which play the role of the neurons along the lamprey's spine. Wells within each linear array are activator-coupled through direct connections (Fig. 2B) and are designed to propagate a chemical wave in one direction as described in the previous section (Fig. 4). In order that the left and right arrays synchronize with a 180° phase difference, the two linear arrays are fabricated side-by-side to create the inhibitory interaction through the PDMS (Fig. 2A). As before, illumination is used to control boundary and initial conditions, as well as to create a pacemaker for each column (Fig. 8A).

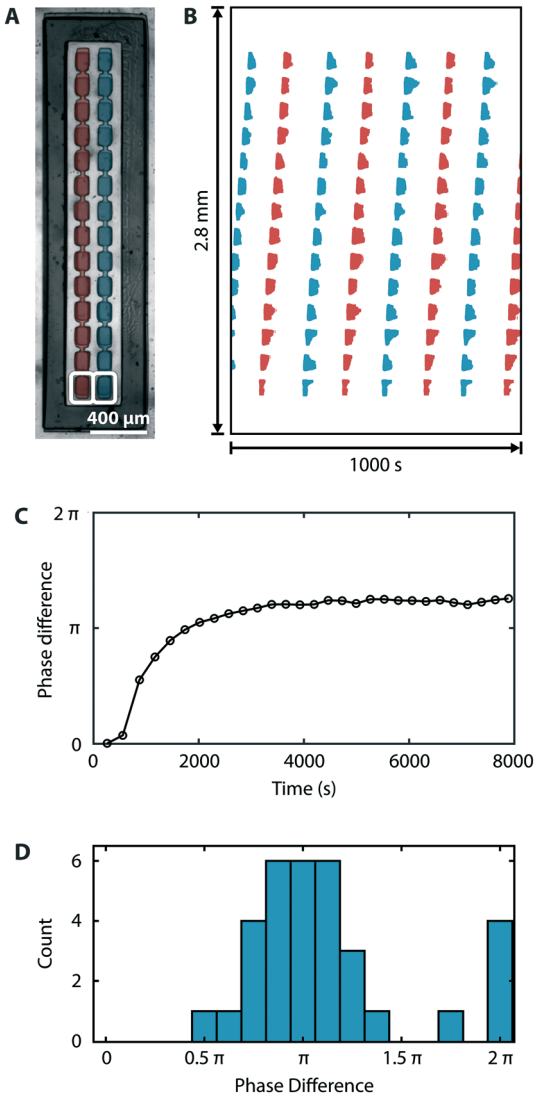

Fig. 8 Bioinspired central pattern generator.[2] (A) Two excitatory coupled linear arrays constructed from PDMS are fabricated side-by-side and filled with BZ solution. The arrays are surrounded by a BZ filled moat to maintain constant chemical boundary conditions. All wells are 120 μm length × 80 μm width × 90 μm height. Connecting channels are 50 μm long, 20 μm wide and 30 μm deep. The two rows of wells are separated by 70 μm of PDMS. Pacemaker wells, uninhibited by light, are indicated by white boxes. See Movie S4.† (B) Space–time plots of the network shown in (A). Two space–time plots are superimposed. Red traces show oscillations of wells that are marked red in (A) (left column), blue traces show oscillations of wells marked in blue (right column). The rows of the space–time plot in (B) are aligned with the rows of the BZ array in (A). Traveling waves within a particular linear array of wells appear as parallel slanted red or blue lines in the space–time plot, indicative of a constant velocity. Oscillations in the two neighboring arrays are anti-phase. (C) Phase difference between pacemaker wells in (A) and (B) *vs.* time. The two arrays start with pacemakers in-phase and gradually evolve to an anti-phase pattern. Linear array separation: 70 μm; (D) steady-state phase difference distribution for 33 experiments.

To demonstrate the robustness of the design of the CPG shown in Fig. 8A, we purposely initiate the system as close to in-phase synchrony as experimentally possible, which is an initial condition as far away from the designed anti-phase dynamical attractor as possible. The space–time plot in Fig. 8B is recorded after the network is in steady state and corresponds closely to the target spatio-temporal pattern of the central pattern generator shown Fig. 1C. The phase difference between the left (red) and right (blue) halves of the central pattern generator *vs.* time shown in Fig. 8C demonstrates that the phase difference between linear arrays grows in time until the twin sides of the CPG phase lock near 180°, which is the designed dynamical attractor; additional experimental observations are shown in the ESI,† Fig. S6. Movie S5† shows the FEM simulations that correspond to the experiments shown in Fig. 8C and Movie S4.† Fig. 8D shows the steady state phase difference between the linear arrays, for 33 separate experiments. Variations away from the desired attractor are due to heterogeneities in the system, our models reproduce this behavior when the boundary conditions are not equal on each side of the arrays. Notably, there is an additional small peak at 0° phase shift, indicative of a second basin of attraction in the network. Our numerical models predict that the in-phase attractor is both small and shallow. The occurrence of this state is therefore controlled by both the initial condition and boundary conditions of the system. In spite of initiating the CPG with the least favorable initial condition possible, the CPG attained the designed attractor 85% of the time, demonstrating design robustness. While the great majority of experiments achieve near anti-phase synchrony, we observe large variability in the time of approach to steady state. We discuss these observations and compare to model results in the ESI,† Fig. S6–S8.

Conclusion

Neural tissue evolved 3.5 billion years after the origin of life, which is a testament to its complexity, and is found in almost all multicellular life, which is a testament to its importance. At the coarsest level of description, neurons are non-linear oscillators that when coupled together in tissue through excitatory and inhibitory connections give rise to complex spatio-temporal patterns. When organized, these patterns are capable of processing and storing sensory information, and actuating musculature. Extrapolating from this general

 This journal is © The Royal Society of Chemistry 2018

definition of a neuronal network as a spatiotemporal pattern generator, we posit these dynamics can be captured on an abiologic reaction–diffusion platform. Here, we report advances in soft lithography that allow the engineering of synthetic reaction–diffusion networks capable of producing a wide variety of spatiotemporal patterns. We employ the well-known oscillatory Belousov–Zhabotinsky reaction and develop methods to create diffusively coupled networks over which we design (i) the topology of the network, the (ii) boundary and (iii) initial conditions, (iv) the volume of each reactor, (v) the coupling strength, and (vi) whether the coupling is of an inhibitory or excitatory nature. It is important to note that the engineering principles we identify are general and can be applied to other oscillatory reaction–diffusion systems.

An application for the reaction–diffusion based networks developed here is to the field of soft robotics, where the central pattern generator will serve as the controller of an artificial musculature comprised of chemomechanical gels coupled to the BZ layer.[40,41] *Soft Robotics*,[42–44] a field at the forefront of engineering and materials science, aims to engineer purely synthetic materials and devices with robust dynamical abilities currently observed only in living matter, such as the undulations of a lamprey[1,2] (Fig. 1). However, the field of soft robotics has focused primarily on developing new, biomimetic methods of actuation while relying on traditional forms of control, while here our control device is based on a neural inspired spatiotemporal paradigm.

In biology, the control network, or nervous system, is distinct from the actuation network, or musculature. This separation of control and actuation in biology has an analogy to the field of electro-mechanical robotics, where control is performed by logic circuits and actuation by electrical motors. Each of these subsystems is complex and presents engineering challenges that require specialized training and focused attention to solve. It is common practice to develop new robotic technologies by taking a three-tiered approach; separately optimize control and actuation, then integrate the two sub-systems. The modular approach has the advantage that many different applications can be built up through the assembly of different combinations of control and actuation systems. Likewise, we adopt a multi-tiered approach to the goal of creating autonomous reaction–diffusion based soft robots. As an application of the reaction–diffusion network technology we developed, we fabricated a controller compatible with soft robotics and demonstrated it had the functionality equivalent to the biologic central pattern generator neural network. As a next step, we envision fabricating an actuation network consisting of poly(*N*-isopropylacrylamide) hydrogels capable of chemomechanical motion based on the BZ reaction.[40,41,45] The ultimate challenge will be transferring the information coded in the dynamical spatiotemporal patterns of compartmentalized chemical reactors into a targeted mechanical response by coupling the central pattern generator demonstrated here to chemomechanical gels that contract in concert with the BZ reaction.[41,45]

Conflicts of interest

There are no conflicts to declare.

Acknowledgements

We thank Xiaotong Geng, Rémi Boros, Matthew Cambria and Ethan Chan for their help as undergraduate researchers during the initial phase of the project. We acknowledge financial support from NSF DMREF-1534890, the U. S. Army Research Laboratory and the U. S. Army Research Office under contract/grant number W911NF-16-1-0094, and the microfluidics facility of the NSF MRSEC DMR-1420382. S. F. and T. L. developed the experimental setup and designed the experiments. T. L. and V. T. fabricated microfluidic devices. T. L. and V. T. performed experiments. T. L. and M. N. analyzed the data. M. N. developed the theory and performed computer simulations. T. L., S. F. and M. N. wrote the manuscript. T. L. and M. N. developed the figures.

References

1 J. D. Murray, *Mathematical biology - I. An Introduction*, Springer, New York, 3rd edn, 2002, ch. 12.
2 A. J. Ijspeert, *Neural Networks*, 2008, **21**, 642–653.
3 A. M. Turing, *Philos. Trans. R. Soc. London, Ser. B*, 1952, **237**, 37–72.
4 A. M. Zhabotinsky, *Dokl. Akad. Nauk SSSR*, 1964, **157**, 392.
5 R. M. Noyes, R. Field and E. Koros, *J. Am. Chem. Soc.*, 1972, **94**, 1394–1395.
6 M. Cross and H. Greenside, *Pattern formation and dynamics in nonequilibrium systems*, Cambridge University Press, Cambridge, UK, New York, 2009.
7 S. H. Strogatz, *Nonlinear dynamics and Chaos: with applications to physics, biology, chemistry, and engineering*, Addison-Wesley Pub., Reading, Mass., 1994.
8 I. Lengyel and I. R. Epstein, *Proc. Natl. Acad. Sci. U. S. A.*, 1992, **89**, 3977–3979.
9 V. Horvath, P. L. Gentili, V. K. Vanag and I. R. Epstein, *Angew. Chem., Int. Ed.*, 2012, **51**, 6878–6881.
10 A. F. Taylor, M. R. Tinsley, F. Wang, Z. Huang and K. Showalter, *Science*, 2009, **323**, 614–617.
11 E. Nakouzi, J. F. Totz, Z. Zhang, O. Steinbock and H. Engel, *Phys. Rev. E*, 2016, **93**, 022203.
12 P. L. Gentili, M. S. Giubila, R. Germani, A. Romani, A. Nicoziani, A. Spalletti and B. M. Heron, *Angew. Chem., Int. Ed.*, 2017, **56**, 7535–7540.
13 K. Torbensen, F. Rossi, S. Ristori and A. Abou-Hassan, *Lab Chip*, 2017, **17**, 1179–1189.
14 N. Tompkins, M. C. Cambria, A. L. Wang, M. Heymann and S. Fraden, *Chaos*, 2015, **25**, 064611.
15 J. Guzowski, K. Gizynski, J. Gorecki and P. Garstecki, *Lab Chip*, 2016, **16**, 764–772.
16 N. Li, N. Tompkins, H. Gonzalez-Ochoa and S. Fraden, *Eur. Phys. J. E: Soft Matter Biol. Phys.*, 2015, **38**, 18.
17 N. Tompkins, N. Li, C. Girabawe, M. Heymann, G. B. Ermentrout, I. R. Epstein and S. Fraden, *Proc. Natl. Acad. Sci. U. S. A.*, 2014, **111**, 4397–4402.

18 J. Delgado, N. Li, M. Leda, H. O. González-Ochoa, S. Fraden and I. R. Epstein, *Soft Matter*, 2011, **7**, 3155–3167.
19 N. Li, J. Delgado, H. O. Gonzalez-Ochoa, I. R. Epstein and S. Fraden, *Phys. Chem. Chem. Phys.*, 2014, **16**, 10965–10978.
20 M. Toiya, H. O. González-Ochoa, V. K. Vanag, S. Fraden and I. R. Epstein, *J. Phys. Chem. Lett.*, 2010, **1**, 1241–1246.
21 A. L. Wang, J. M. Gold, N. Tompkins, M. Heymann, K. I. Harrington and S. Fraden, *Eur. Phys. J.: Spec. Top.*, 2016, **225**, 211–227.
22 K. Torbensen, S. Ristori, F. Rossi and A. Abou-Hassan, *J. Phys. Chem. C*, 2017, **121**, 13256–13264.
23 R. Tomasi, J.-M. Noel, A. Zenati, S. Ristori, F. Rossi, V. Cabuil, F. Kanoufi and A. Abou-Hassan, *Chem. Sci.*, 2014, **5**, 1854–1859.
24 K. Miyakawa, T. Okano and S. Yamazaki, *J. Phys. Soc. Jpn.*, 2013, **82**, 034005.
25 T. Okano and K. Miyakawa, *Phys. Rev. E: Stat., Nonlinear, Soft Matter Phys.*, 2009, **80**, 026215.
26 B. T. Ginn, B. Steinbock, M. Kahveci and O. Steinbock, *J. Phys. Chem. A*, 2004, **108**, 1325–1332.
27 P. R. Buskohl and R. A. Vaia, *Sci. Adv.*, 2016, **2**, e1600813.
28 J. C. McDonald, D. C. Duffy, J. R. Anderson, D. T. Chiu, H. Wu, O. J. Schueller and G. M. Whitesides, *Electrophoresis*, 2000, **21**, 27–40.
29 O. Qi, W. Y. Tam, P. DeKepper, W. D. McCormick, Z. Noszticzius and H. L. Swinney, *J. Phys. Chem.*, 1987, **91**, 2181–2184.
30 V. K. Vanag and I. R. Epstein, *J. Chem. Phys.*, 2009, **131**, 104512.
31 N. Tompkins and S. Fraden, *Am. J. Phys.*, 2016, **84**, 150–158.
32 A. Toth, V. Gaspar and K. Showalter, *J. Phys. Chem.*, 1994, **98**, 522–531.
33 S. Martens, J. Löber and H. Engel, *Phys. Rev. E*, 2015, **91**, 022902.
34 A. Ziepke, S. Martens and H. Engel, *J. Chem. Phys.*, 2016, **145**, 094108.
35 L.-Q. Zhou, I. Cassidy, S. C. Müller, X. Cheng, G. Huang and Q. Ouyang, *Phys. Rev. Lett.*, 2005, **94**, 128301.
36 N. Manz and O. Steinbock, *Chaos*, 2006, **16**, 037112.
37 G. Bordyugov, N. Fischer, H. Engel, N. Manz and O. Steinbock, *Phys. D*, 2010, **239**, 766–775.
38 S. Grillner, *Neuron*, 2006, **52**, 751–766.
39 A. J. Ijspeert, *Science*, 2014, **346**, 196–203.
40 R. Yoshida, T. Takahashi, T. Yamaguchi and H. Ichijo, *J. Am. Chem. Soc.*, 1996, **118**, 5134–5135.
41 Y. Zhang, N. Zhou, N. Li, M. Sun, D. Kim, S. Fraden, I. R. Epstein and B. Xu, *J. Am. Chem. Soc.*, 2014, **136**, 7341–7347.
42 B. Trimmer, *Soft Robotics*, 2013, **1**, 1–4.
43 E. M. Izhikevich, *Dynamical systems in neuroscience: the geometry of excitability and bursting*, MIT Press, Cambridge, Mass., 2007.
44 D. Rus and M. T. Tolley, *Nature*, 2015, **521**, 467–475.
45 R. Yoshida, *Polym. J.*, 2010, **42**, 777–789.

This journal is © The Royal Society of Chemistry 2018